

## A New Passive Tomography of the Aigion Area (Gulf of Corinth, Greece) from the 2002 Data Set

S. GAUTIER,<sup>2</sup> D. LATORRE,<sup>3</sup> J. VIRIEUX,<sup>1</sup> A. DESCHAMPS,<sup>1</sup> C. SKARPELOS,<sup>4</sup> A. SOTIRIOU,<sup>4</sup>  
A. SERPETSIDAKI,<sup>4</sup> and A. TSELENTIS<sup>4</sup>

*Abstract*—We present the results of a tomographic study performed in the framework of the 3F-Corinth project. The aim of this work is to better understand the rifting process by imaging the crustal structure of the western Gulf of Corinth. Forty-nine stations were deployed for a period of six months, allowing us to monitor the microseismicity. Delayed P and S first-arrival times have been simultaneously inverted for both hypocenter locations and 3-D velocity distributions. We use an improved linearized tomography method based on an accurate finite-difference travel-time computation to invert the data set. The obtained Vp and Vs models confirm the presence of a two-layer vertical structure characterized by a sharp velocity gradient lying at 5–7 km depth, which may be interpreted as a lithological contrast. The shallower part of the crust (down to 5 km depth) is controlled by the N-S extension and lacks seismicity. The deeper part (7–13 km depth) matches the seismogenic zone and is characterized by faster and more heterogeneous anomalies. In this zone, the background seismicity reveals a low-angle active surface dipping about 20° toward the north and striking WNW-ESE. The position of this active structure is consistent with both high Vp/Vs and low Vp.Vs anomalies identified at 8–12 km depth and suggesting a highly fractured and fluid-saturated zone. Both the geometry of the active structure beneath the gulf and the presence of fluids at 8–12 km depth are in accordance with a low-angle detachment model for the western part of the Gulf of Corinth.

**Key words:** Gulf of Corinth, rifting, low-angle detachment, seismic tomography, Vp/Vs, Vp.Vs.

### 1. Introduction

The Gulf of Corinth (Greece) is a continental rift, which has long been recognized as one of the most active regions in Europe. The historical seismicity is very high: five events of magnitude larger than 5.8 have been observed in this area within the last 40 years. The last event was the Ms = 6.2, 15 June 1995, Aigion earthquake

---

S. Gautier and D. Latorre formerly at Géosciences Azur

<sup>1</sup>Géosciences Azur, Université de Nice - Sophia Antipolis/CNRS, 06560, Valbonne, France.

<sup>2</sup>Laboratoire de Tectonophysique, Université de Montpellier 2/CNRS, Place Eugène Bataillon, CC049, 34095, Montpellier cedex 5, France.

<sup>3</sup>Instituto Nazionale di Geofisica e Vulcanologia, CNT, Roma, Italy.

<sup>4</sup>Patras Seismological Laboratory, University of Patras, Greece.

(BERNARD *et al.*, 1997), located in the western part of the gulf where we focus our study.

Despite a large amount of recent tectonic, geodetic and seismic observations, there is considerable debate concerning the rifting process. The presence of a low-angle detachment zone (RIGO *et al.*, 1996; SOREL, 2000) and the rise of the brittle-ductile transition up to 10 km depth (HATZFELD *et al.*, 2000) are the two main tectonic models proposed to explain both the distribution of the seismicity at depth and the focal mechanisms. The understanding of the rifting process first requires a better-constrained structural model of the mid-crust for the Corinth region.

In 1991 a two-month-long passive seismological experiment took place in the western part of the gulf, around the city of Aigion (Fig. 1). The collected data set was used by RIGO *et al.* (1996) for seismotectonic interpretation. This data set has been used as well to perform tomographic studies. First results were obtained by LE MEUR *et al.* (1997) and new velocity models were constructed by LATORRE *et al.* (2004b) using an improved tomographic technique. LATORRE *et al.* (2004b) found a two-layer vertical structure and the presence of a high  $V_p/V_s$  anomaly at depth, suggesting a possible role of fluids in the rifting process. Despite important results, the quality of the 1991 data is limited because of many vertical single component (1C) stations, imposing a major limitation in constraining the mid-crust structure and the seismicity distribution.

A new passive seismological experiment (3F-Corinth European Project) was performed from November 2001 until June 2002 around the Aigion area. The new data set has been collected with a homogeneous and efficient instrumental network (Fig. 1). The aim of this seismological experiment is to provide 3-D and high-resolved images of the mid-crust in order to shed light on our understanding of the rifting process. In this paper, we present the results of a tomographic study obtained from the large 2002 data, using the technique presented by LATORRE *et al.* (2004b), VANORIO *et al.* (2005), and MONTEILLIER *et al.* (in press).

## 2. Geologic Setting

The Gulf of Corinth is located in the Aegean area, in the western part of the Mediterranean region. The Aegean is bounded at the south and west by the Hellenic arc. The African plate subducts beneath the Aegean along the Hellenic arc with a rate of  $\sim 0.5 \text{ cm.yr}^{-1}$  (MCCLUSKY *et al.*, 2000). At the east of the Aegean, the Anatolian block is laterally extruded westward along the North Anatolian fault.

Extension in the Aegean region started in the Miocene times (LE PICHON and ANGELIER, 1979; JOLIVET *et al.*, 1994; ARMIJO *et al.*, 1996). This extension could be related to both a gravitational collapse of the Hellenides mountains (LE PICHON *et al.*, 1995; JOLIVET, 2001) and a lithospheric thinning in the Aegean backarc zone (DOUTSOS *et al.*, 1988). A series of periodic graben structures seems to accommodate

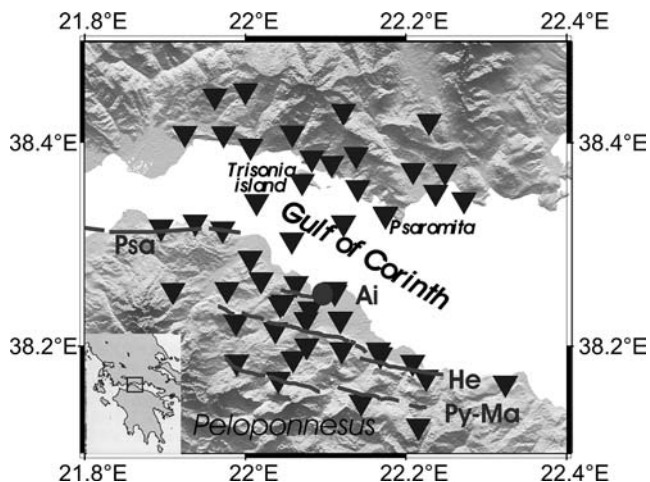


Figure 1

Map of the western Gulf of Corinth. The selected area is shown on the left bottom corner. The location of the town of Aigion is indicated with the dark dot. The complete network used during the 2001–2002 experiment is represented with triangles and major faults are drawn in dark grey (Psa: Psathopyrgos fault; Ai: Aigion fault; He: Heliki fault and Py-Ma: Pyrgaki-Mamoussia fault).

a part of this deformation (ARMIJO *et al.*, 1996; TIBERI *et al.*, 2001). In this paper, we focus on one of the most active of these structures: the Gulf of Corinth.

The Gulf of Corinth, which separates the Peloponnese from continental Greece, is a 110 km-long, N120°E oriented asymmetrical graben, bounded by quaternary E-W normal faults (Fig. 1). The extension is N10° and GPS measurements show that its rate is more rapid in the west (1.6 cm.yr<sup>-1</sup> at Aigion) than in the east (1.1 cm.yr<sup>-1</sup> at Xilocastro, 50 km eastward from Aigion) (BRIOLE *et al.*, 2000; AVALONE *et al.*, 2004). The most active faults crop out on the southern uplifted side of the Gulf with a dip of 50–60° toward the north. These active faults correspond to a well-organized *en echelon* system, with a characteristic length of 15–25 km (ARMIJO *et al.*, 1996). On the contrary, some smaller antithetic faults can be found on the northern subsided coast.

The geological structure around the gulf region results from the E-W Cenozoic Alpine compression which gave rise to the Hellenic mountains (JACOBSHAGEN *et al.*, 1978). The Hellenic mountains are comprised of a stack of Mesozoic nappes with a NNW-SSE trend. In our studied area, the Pindos series corresponds to the shallowest unit. It consists of deep-water carbonates with a minimum thickness of 3.5 km (AUBOUIN *et al.*, 1962). Magneto-telluric modelling suggests that the Pindos unit is highly fractured up to 3 km depth (PHAM *et al.*, 2000). This nappe overthrusts the Gavrovo-Tripolitza series composed of about 2.5-km-thick carbonate platform sediments (AUBOUIN *et al.*, 1962). Both the Pindos and the Gavrovo-Tripolitza series extend on the southern and the northern edges of the Gulf (DOUTSOS and POULIMENOS, 1992). Below these nappes, a metamorphic unit called the Phyllite series is likely be

encountered (JACOBSHAGEN *et al.*, 1978; DORNSIEPEN *et al.*, 2001). The Phyllite series consists of an alternation of quartzites, phyllites and schists (DORNSIEPEN *et al.*, 2001). This unit crops out on a tectonic window located on the southern side of the studied area (XYPOLIAS and KOUKOUVELAS, 2001) while the extent of this nappe toward the north is not clearly known. Finally, field observations point out a 1-km-thick synrift sedimentary sequence in north Peloponnesus (DOUTSOS and POULIMENOS, 1992; FLOTTÉ and SOREL, 2001) whereas no evidence of synrift deposits was found in the northern edge of the Gulf (DOUTSOS and POULIMENOS, 1992). Moreover, east of our studied area, reflection seismic images show that the synrift sediment basin beneath the Gulf reaches a depth of 2.5 km (SACHPAZI *et al.*, 2003).

Gravity data suggest the presence of a NW-SE trending crustal thinning beneath the northern side of the Gulf of Corinth, probably related to the Miocene extension (TIBERI *et al.*, 2001). Some authors assume that the Gulf structure has been reactivated in Quaternary times ( $\sim 1$  Ma) by the southwestward propagation of the North Anatolian fault (ARMIJO *et al.*, 1996). This led to a westward propagation of the rift (CLARK *et al.*, 1997), which can be a possible cause of the high extension rate observed in this area (AVALLONE *et al.*, 2004). Both gravity and seismological data (TIBERI *et al.*, 2000, 2001) also indicate an offset between the crustal thinning and the location of the rift at the surface that becomes maximum in the western part of the Gulf. This suggests a modification of the rupture propagation between the Miocene and the Quaternary times. Changes in boundary conditions or pre-existing crustal heterogeneities may account for this offset (TIBERI *et al.*, 2001).

In the western part of the Gulf, the microseismicity is mainly distributed along a subhorizontal north-dipping trend, located at about 6–12 km depth (RIGO *et al.*, 1996; LATORRE *et al.*, 2004b; LYON-CAEN *et al.*, 2004). RIGO *et al.* (1996) interpret the seismogenic zone as a north-dipping detachment structure that could accommodate the deformation in this area. Fault plane solutions indicating the presence of an active low-angle dipping structure at depth are consistent with this tectonic model (RIETBROCK *et al.*, 1996; BERNARD *et al.*, 1997). Some authors also hypothesize a connection between this low-angle structure and the steeper north-dipping normal faults that crop out on the southern edge of the Gulf (RIETBROCK *et al.*, 1996; RIGO *et al.*, 1996; BERNARD *et al.*, 1997; SOREL, 2000; FLOTTÉ and SOREL, 2001). HATZFELD *et al.* (2000) propose an alternative model suggesting that the background microseismicity marks a brittle-ductile transition zone, without any peculiar structure. In their interpretation, microearthquake mechanisms with a dip steeper than  $15^\circ$  may be related to small faults located at the base of the brittle-crust.

### 3. The 2002 Passive Tomographic Experiment

In the framework of the 3F-Corinth project, a dense passive seismological experiment took place around the Aigion area, in the western part of the Gulf of

Corinth, from November 2001 until June 2002. From February until June 2002, the network was made up of 30 3C L22 2 Hz digital and 19 3C CMG40 60 s digital stations using GPS time (temporary stations and CRL permanent stations (LYON-CAEN *et al.*, 2004)) deployed on both sides of the Gulf. The complete network is represented in Figure 1. The distance between two stations is around 5 km. During March-April, three 3C ocean-bottom seismometers were deployed in the center of the Gulf for a one-month period, allowing an increase of the ray coverage in the study area. Compared with the 1991 experiment, the quality of the new collected data set was improved thanks to a geographic and instrumental homogeneity, improved timing, improved station locations, and 3C sensors.

A mean of 400 events per month was recorded during this dense passive experiment. Both P- and S-first arrival times were handpicked and an initial location was obtained using the 1-D model proposed by RIGO *et al.* (1996), assuming an *a priori*  $V_p/V_s$  ratio of 1.8. In order to obtain a more reliable and uniform tomographic data set, we have performed a selection using different criteria. First, we selected first arrival times that have high-quality readings by following the pick qualities given by the operator ( $w_P \leq 2$ ,  $w_S \leq 3$ ). Then, we removed events with a greatest angle without observation (GAP) higher than  $180^\circ$  and with a focal depth lower than 17 km, i.e., the maximum depth of the tomographic velocity model. Finally, only events with more than 8P and 4S picked phases and with a rms travel-time residual value lower than 0.5 s were kept for this study. The resulting reduced data set consists in 451 events with 9236 P- and 7523 S-first arrival times.

Figures 2 and 3 show the initial velocity distribution and hypocenters localized in the 1-D model of RIGO *et al.* (1996). In accordance with previous results, we note that the microseismicity lies between 4 km and 15 km depths and is particularly concentrated between 6 km and 12 km depths (RIGO *et al.*, 1996; LATORRE *et al.*, 2004b; LYON-CAEN *et al.*, 2004). Pictures also indicate a lack of seismicity above 4 km depth.

#### 4. The 3-D Delayed Travel-time Tomography

##### 4.1 Methodology

We use a 3-D delayed travel-time tomography method to invert simultaneously the velocity distribution and the hypocenter parameters (AKI and LEE, 1976; SPAKMAN and NOLET, 1988; BENZ *et al.*, 1996; SPENCER and GUBBINS, 1980; THURBER, 1992). The inversion method provides a smooth velocity model estimated on a 3-D, regularly spaced, rectangular grid. Sharp discontinuity imaging may be performed by converted phase analysis (LATORRE *et al.*, 2004a) allowing detection of small-scale discontinuities, as active fault planes or other structural interfaces (BENZION and MALIN, 1991). A comprehensive description of the tomographic method and its linearized iterative scheme is given by LATORRE *et al.* (2004b).

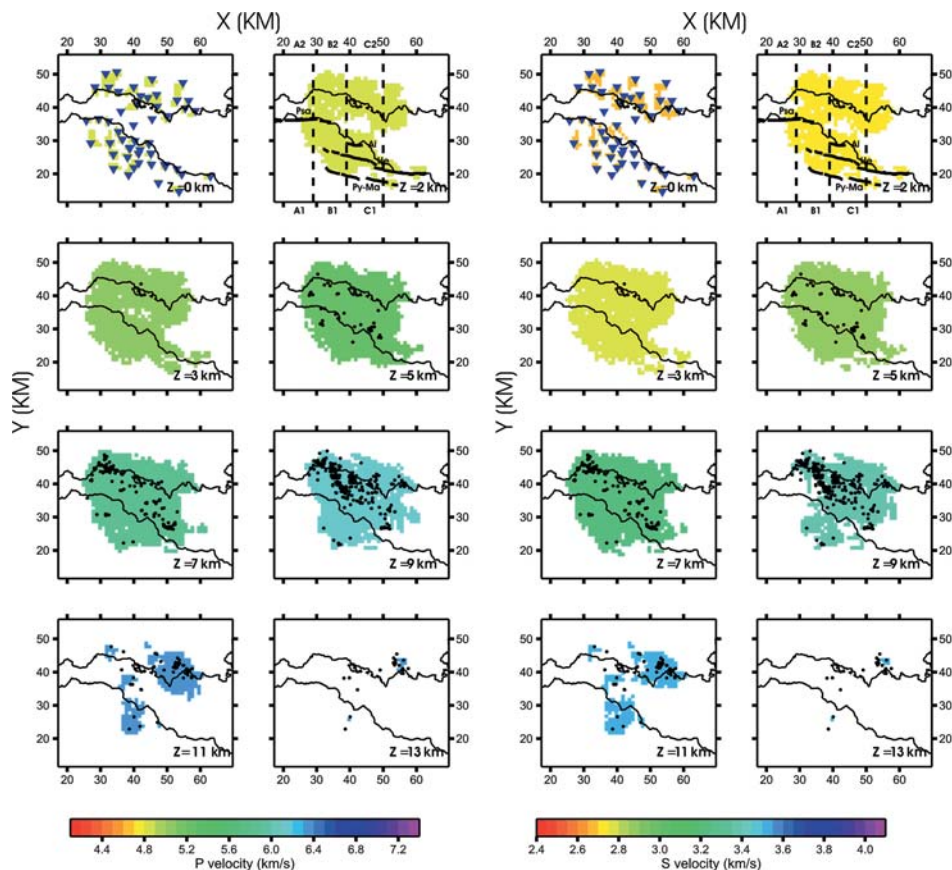


Figure 2

Hypocenters localized in the 1-D model ( $V_p$  on the left and  $V_s$  on the right) and used for the tomographic study are presented on map views at different depths ranging from 0 km to 13 km. Distances are represented in the X-Y coordinate system derived from the Universal Transverse Mercator (UTM) projection (zone 34) and a local origin point (longitude =  $21.6^\circ\text{E}$  and latitude =  $38^\circ\text{N}$ ) is used for plotting presentation. Events located in a range of 1 km around each layer are displayed (dark dots). Stations are plotted on the first section (blue triangle) whereas the major faults are drawn on the second map.  $1\text{ km}^3$  cells with no ray coverage have been masked. The color scale indicates the absolute velocity from the lowest value in red to the highest value in blue.

At each iteration, we compute travel-times by solving the Eikonal equation with a finite-difference algorithm (PODVIN and LECOMTE, 1991). Rays are obtained using an *a posteriori* ray-tracing method that is based on time gradients. More precise travel-times and partial derivatives, both for slowness fields and for hypocenter parameters, are evaluated along the ray paths. As proposed by LE MEUR *et al.* (1997), a normalization/scaling of the derivative matrix is performed in order to control the quality of the recovered parameters. The aim of this operation is to

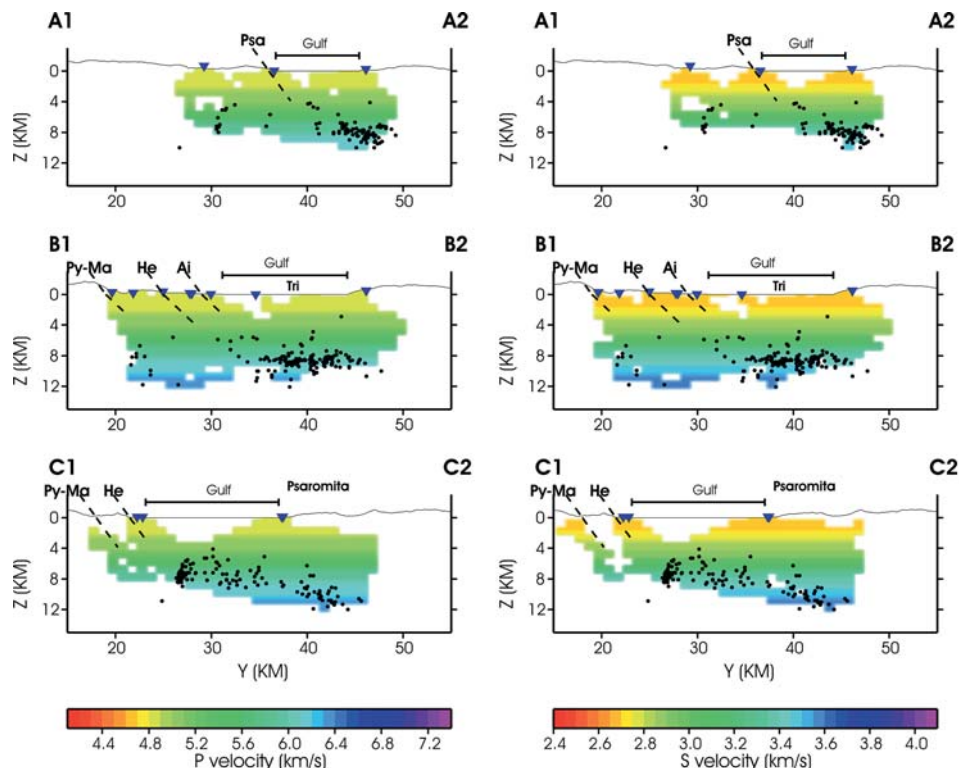


Figure 3

S-N sections of the initial microseismicity localized in the 1-D model ( $V_p$  on the left and  $V_s$  on the right). The location of each S-N section is indicated on Figure 2. Earthquakes (dark dots) that are located in a 3.5 km wide area around each section are plotted. Major normal faults are displayed on the pictures. We used the same mask as in Figure 2.

remove influences of parameter units and also to take into account the sensitivity of the data to each class of parameters. Because this procedure is configuration dependent, synthetic tests with the real source-receiver distribution were performed to estimate values of the weightings. Residual weighting of the data set is also used in our tomography to eliminate the outliers. Finally, the scaled and weighted linear system is solved by means of the *LSQR* method (PAIGE and SAUNDERS, 1982) and both the velocity models and the hypocenter parameters are updated. For inversion regularization, we use a damping factor determined through synthetic tests. For *LSQR*, 70 internal iterations allow a good accuracy of recovered parameters. The total number of iterations for the global tomographic procedure with new ray tracing is fixed to 25 iterations. An *a posteriori* analysis of both misfit and model perturbation functions shows that the convergence is usually reached after 10 iterations (Fig. 7).

#### 4.2 Parameterization for the 2002 Experiment

The tomographic inversion is applied over a  $56 \text{ km} \times 56 \text{ km}$  area, which includes all the stations. The velocity model is defined up to 17 km depth in order to include all the ray paths. In order to compare the 2002 tomographic results with those of 1991, we use the same grid as the optimal one defined for the 1991 tomographic study (LATORRE *et al.*, 2004b). The distance between grid points is 7 km in the two horizontal X and Y directions and 2 km in the vertical Z direction.

We fix the different weightings and the damping parameter through synthetic tests using the real event-station geometry. Synthetic velocity models were obtained by adding a central positive anomaly ( $400 \text{ km.s}^{-1}$  for  $V_p$  and  $200 \text{ km.s}^{-1}$  for  $V_s$ ) within a homogeneous distribution ( $4000 \text{ km.s}^{-1}$  for  $V_p$  and  $2000 \text{ km.s}^{-1}$  for  $V_s$ ). Theoretical travel-times were computed in these velocity models in order to generate the synthetic data set. We added a noise term to the synthetic arrivals from a uniform distribution between  $-0.05 \text{ s}$  and  $0.05 \text{ s}$ . This simulates systematic errors associated with the arrival times as the picking ones. In order to obtain new hypocenter locations, events were relocated in the initial model defined as the homogeneous velocity distribution. Tomographic inversions were performed for different sets of weightings and damping parameter. For the estimation of the optimal parameterization, we analyze the quality of both the reconstructed velocity models and the retrieved hypocenter parameters. A low final rms value is an additional criterion. Analyzing the test results, we estimated that the optimal set of weightings for the 2002 tomographic study is 1 for P waves, 2 for S waves, 5 for both the location and the origin time of earthquakes and finally 0.5 for the damping parameter. These results are consistent with the set of parameters used by LATORRE *et al.* (2004b) for the 1991 data set corresponding to a damping value 0.5 and weights equal to 1 for P waves, 1.25 for S waves and 5 for the hypocenter parameters. The strong difference of the weighting factor for S waves illustrates the more homogeneous and dense S-coverage (very high number of S-pickings) of the 2002 data set with respect to that of 1991.

#### 4.3 The Initial Velocity Model

We start with a 1-D velocity model: the P-velocity model proposed by RIGO *et al.* (1996). The corresponding initial S-velocity model is directly obtained from the P-velocity distribution assuming a  $V_p/V_s$  ratio of 1.8.

Because the initial model has a strong influence in linearized iterative inversions (KISSLING *et al.*, 1994), we analyze the sensitivity of the 2002 tomographic results with respect to the starting model. No specific estimation of the model uncertainty was quantified in this study because the medium is insufficiently sampled to give relevant results (MOSEGAARD and TARANTOLA, 1995). The procedure consists in testing many possible starting 1-D models to assess the robustness of the tomographic results. We defined an upper limit

( $+1000 \text{ km.s}^{-1}$ ) and a lower limit ( $-1000 \text{ km.s}^{-1}$ ) around the initial P-velocity model, after which, inversions are performed for 400 1-D models randomly obtained in this given domain, using the real station-event configuration and the optimal parameterization.

Results are presented in Figure 4. The dense heterogeneous distribution of initial rms values (from 0.16 s to 0.75 s) confirms a good sampling of the 1-D starting model space. The 400 final weighted rms values are almost identical, suggesting that there are no important differences in the recovered models. We may deduce that the tomographic results are rather independent of the initial reference in the range of 1-D tested models. Because the model proposed by RIGO *et al.* (1996) gave both the lowest initial and the lowest final weighted rms values, it seems to be the most suitable model among the 400 tested to provide reliable tomographic images.

#### 4.4 Resolution Estimation

We perform checkerboard and spike anomaly tests in order to assess resolution of the tomographic models. Spike tests may be used for the resolution matrix reconstruction for both velocity and earthquake parameters, whereas checkerboard tests provide a global and quick insight of the local resolution length by examining the degree of smearing of the velocity patterns. Checkerboard tests are a practical way of defining the minimum anomaly size that is expected to be resolved in tomographic inversions. This is an *a posteriori* procedure because the final tomographic model is required for performing the checkerboard tests.

First, an input model is constructed by adding a velocity perturbation to the final tomographic velocity models ( $400 \text{ km.s}^{-1}$  for Vp and  $200 \text{ km.s}^{-1}$  for Vs). We verify that the velocity perturbation is strong compared to the numerical noise level and also small enough to avoid noticeable disturbances in the ray coverage. Synthetic travel-times are computed in this new input model using the 2002 source-receiver geometry. In addition, a noise term is added to the synthetic data set from a uniform distribution between  $-0.05 \text{ s}$  and  $0.05 \text{ s}$ . This simulates errors in the arrival times such as for example picking errors. The resulting synthetic data set is then inverted using the same procedure and parameterization that was used for the real data. Finally, the recovered velocity is compared to the input model in order to estimate the model resolution for some parameters like the amplitude, the location, the size and the shape of the reconstructed anomalies, as well as earthquake parameters.

We performed several checkerboard tests for input anomalies of different sizes and locations. The smaller synthetic pattern anomaly corresponds to  $7 \times 7 \times 2 \text{ km}^3$ , i.e., the spacing of the inversion grid. Figure 5 displays the results related to this smaller pattern in order to illustrate that the data set is able to reconstruct the checkerboard anomaly. The velocity perturbation beneath the seismic network is well resolved for both Vp and Vs between the depths of 1 km and 9 km. The

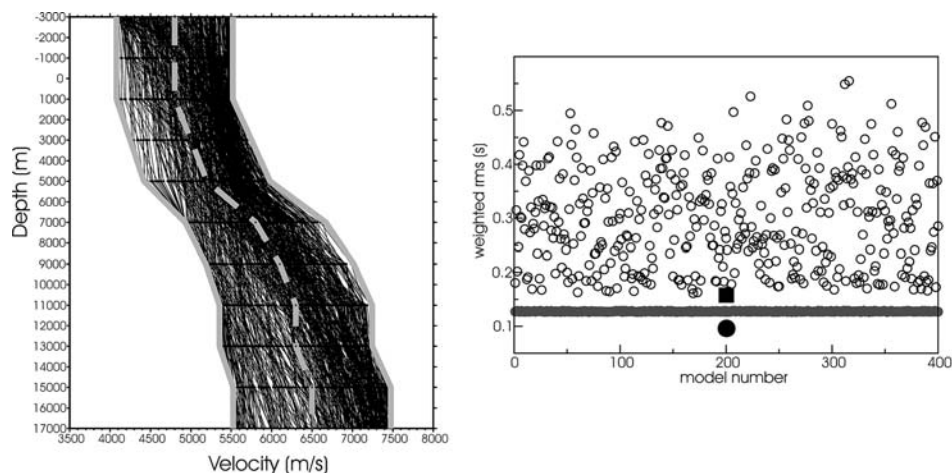


Figure 4

Sensitivity test performed for the initial 1-D model. The panel on the left shows the 400 random 1-D initial models. The dashed line indicates our selected 1-D-model (RIGO *et al.*, 1996) and the grey lines delineate the sampling space. The panel on the right presents the initial weighted rms corresponding to the 400-tested 1-D models (black circles) and the final weighted rms values (grey circles). The rms values for our selected 1-D model are indicated with a square for the initial one and with a circle for the final one.

images show a poor resolution below 11 km depth and at the surface (the  $-1$  km layer), which may be a consequence of the weaker ray coverage. The smearing detected at 11 km depth is probably also due to poor ray sampling. One has to be aware of this maximum depth resolution for geodynamic interpretations.

To illustrate the resolution of our tomographic results, spike tests corresponding to different areas of the inversion grid are performed. Ideally, the resolution matrix is estimated by performing a spike test on each node of the inversion grid (LATORRE *et al.*, 2004b). In our case, the resolution matrix was not entirely computed but the analysis was focused on specific nodes related to the main anomalies observed in the tomographic model. This approach allows us to assess the resolution of different areas for the interpretation of the tomographic images. Taking into account the previous results, spikes have been distributed at different depth ranging from 3 km to 11 km depths. Figure 6 presents results for positive spikes but similar results have also been obtained for negative ones. Spikes located at 7 km depth are well recovered in shape and in position. At 9 km and 11 km depths, the location of the heterogeneities is correctly resolved, although the amplitude is  $\sim 50\%$  lower in average. We found that the poor-resolved spike located at 3 km depth is smeared up. This demonstrates the capability of the data set to resolve velocity anomalies located beneath the seismic network between 3 km to 11 km depth.

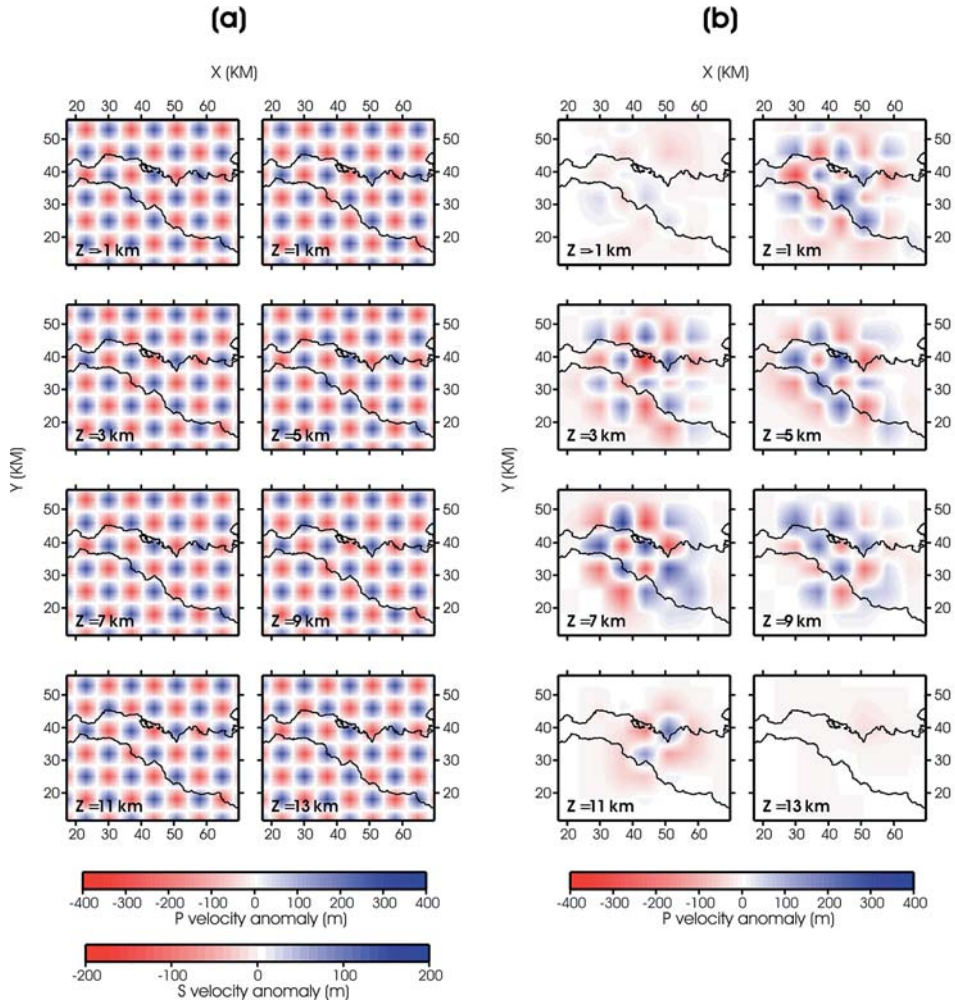


Figure 5

Checkerboard tests for both P- and S-velocity models. (a) Velocity perturbation for P waves ( $\pm 400$  m/s) and S-waves ( $\pm 200$  m/s) added to the 3-D tomographic models. The P- and S-reconstructed patterns are shown respectively in panels (b) and (c).

### 5. Results of the Tomography

We present the tomographic solution obtained after ten iterations. The convergence history (Fig. 7) points out that few modifications of the tomographic model occur after this iteration. The weighted root-mean-squares residual decreases from 162 ms to 106 ms, i.e., a reduction of about 34% of the weighted rms. Both the velocity models ( $V_p$  and  $V_s$ ) and the earthquake locations are shown in Figure 8. In

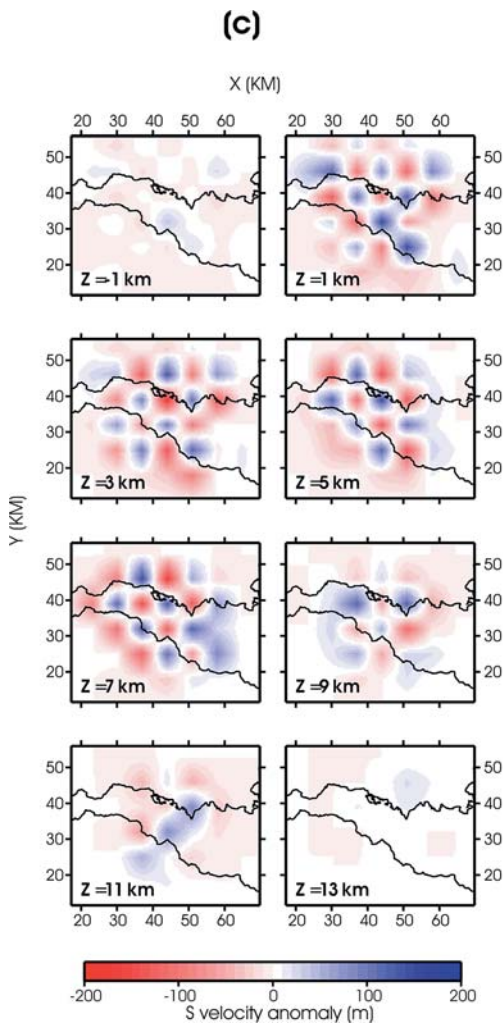


Figure 5  
(Contd.)

addition to the map views, the results are also presented along three S-N vertical sections (Fig. 9), corresponding to different areas of the Gulf region, from the west to the east. Their locations are indicated by dotted lines on the map views.

### 5.1 The P- and S-velocity Models

The velocity models show a two-layer vertical structure occurring at a regional scale. A comparison between initial and final mean velocity profiles (Fig. 10) confirms an important increase of the velocity gradient at 5–7 km depth (from

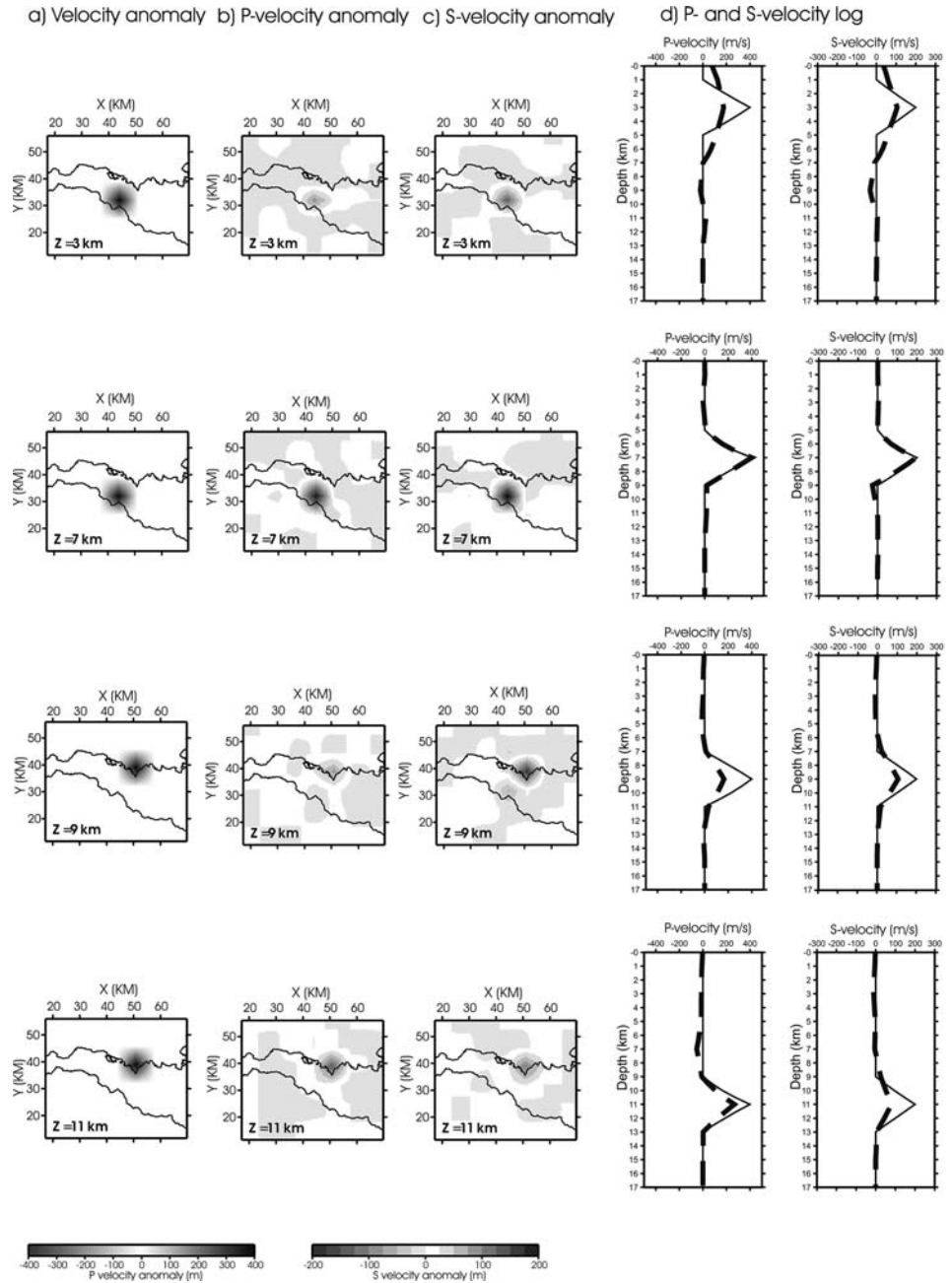


Figure 6

Spike tests for both P- and S- velocity models. Spikes are positioned at different depths ranging from 3 km (top) to 11 km (bottom). The different panels show: (a) Velocity perturbation for P-waves ( $\pm 400$  m/s) and S-waves ( $\pm 200$  m/s) added to the 3-D tomographic models, (b) and (c) the P- and S-reconstructed patterns, and (d) the P- and S-velocity logs corresponding to the spike positions.

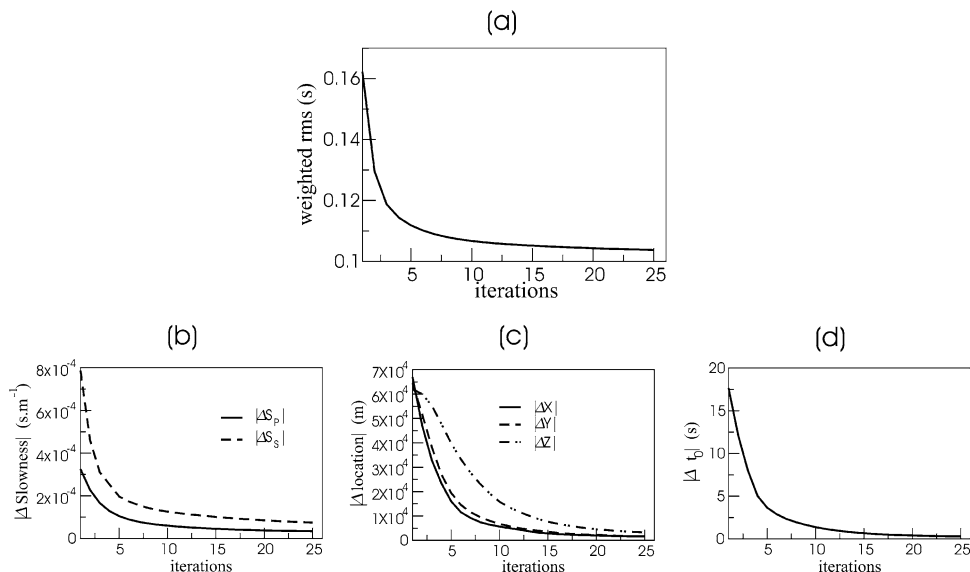


Figure 7

Representation of the convergence history of the tomographic inversion: (a) The misfit function, (b) the total model perturbation norm by step, (c) and (d) the total hypocenter parameters perturbation norm, respectively the event locations and the origin time. We assume that the convergence is reached when the perturbation of the different class of parameters is less than  $\sim 20\%$ .

$5.1 \text{ km.s}^{-1}$  to  $6 \text{ km.s}^{-1}$  for  $V_p$  and from  $2.9 \text{ km.s}^{-1}$  to  $3.4 \text{ km.s}^{-1}$  for  $V_s$ ). This sharp increase seems to be more accentuated for  $V_p$ . S-N sections point out a slight lateral variation of the location of this vertical transition.

Between depths of 0 km and 5 km, the reconstructed P and S models reflect similar velocity patterns. In particular, images point out a low-velocity anomaly ( $4.3 \text{ km.s}^{-1}$  for the P waves and  $\text{km.s}^{-1}$  for the S waves) which correlates well with the graben axis orientation. This zone is bounded by the Heliki fault and the Pyrgaki-Mamoussia fault on the southern side of the Gulf. Around this anomaly, the velocity distribution is more homogeneous ( $5.2 \text{ km.s}^{-1}$  for P waves and  $3 \text{ km.s}^{-1}$  for S waves) with less pronounced lateral variations.

Between 7 km and 13 km depth, the velocity fields are completely distinct in shape, in values and in position from the shallower one. The velocity distribution manifests lateral variations that are uncorrelated with the surface structures. We also note that the P- and S-velocity models display different patterns. For example, at 7 km depth, images show that high velocity anomalies are located on the northern side of the Gulf for the P fields whereas high velocity anomalies are mainly localized on the southern side for the S fields. However, the three S-N sections reveal a low P- and S- velocity anomaly located at 8–12 km depth beneath the northern side of the Gulf, near the Psaromita peninsula.

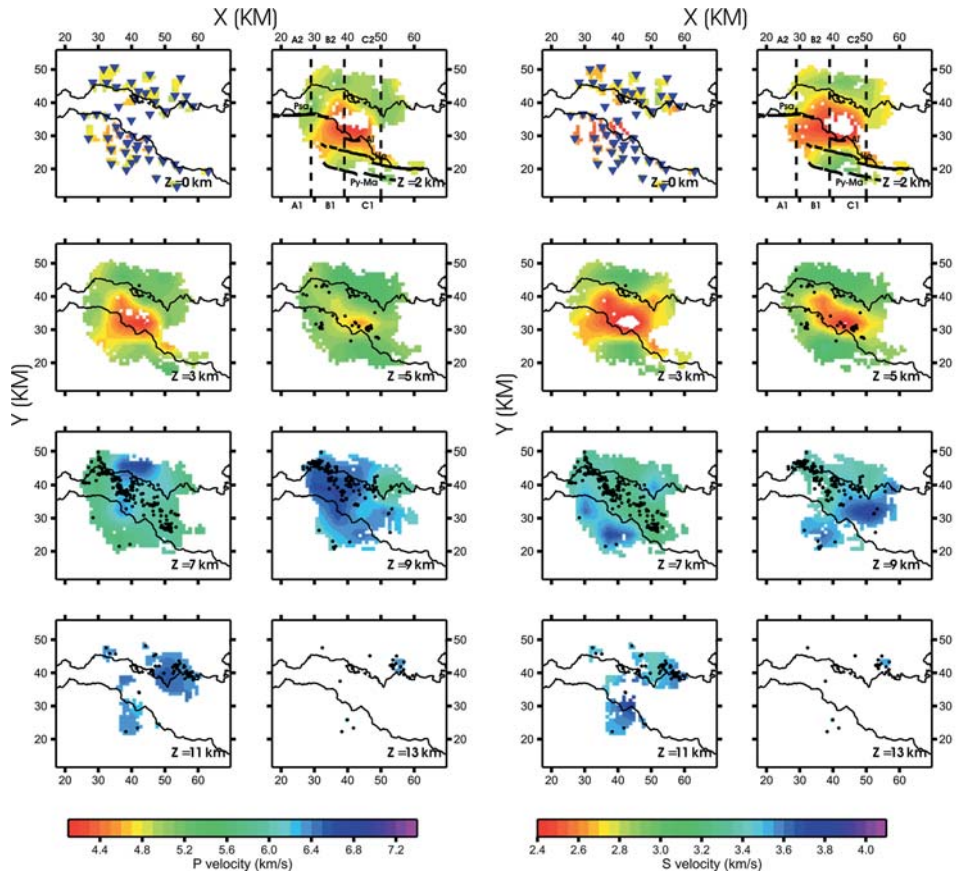


Figure 8

Presentation of the final tomographic results on map views at different depths ranging from 0 km to 13 km with the same caption as in Figure 2.  $V_p$  is presented on the left side and  $V_s$  on the right side.

### 5.2 Event Locations

The final location of the events is indicated on both map views (Fig. 8) and S-N sections (Fig. 9). In comparison with the initial locations, the tomographic results provide a narrow picture of the microseismicity. Event collapse and certain trends in the microseismicity distribution can be identified.

The first result is a lack of events in the shallower zone, between 0 km and 5 km depths. Both map views and S-N sections indicate that the microseismicity is concentrated in the deeper part of the model, between 6 km and 12 km depth. On the map view, at 7 km depth, we observe that earthquakes are concentrated in the center of the Gulf and aligned along a  $120^\circ$  NW-SE direction similar to the orientation of the Gulf. Event distribution moves from S-W to N-E with almost

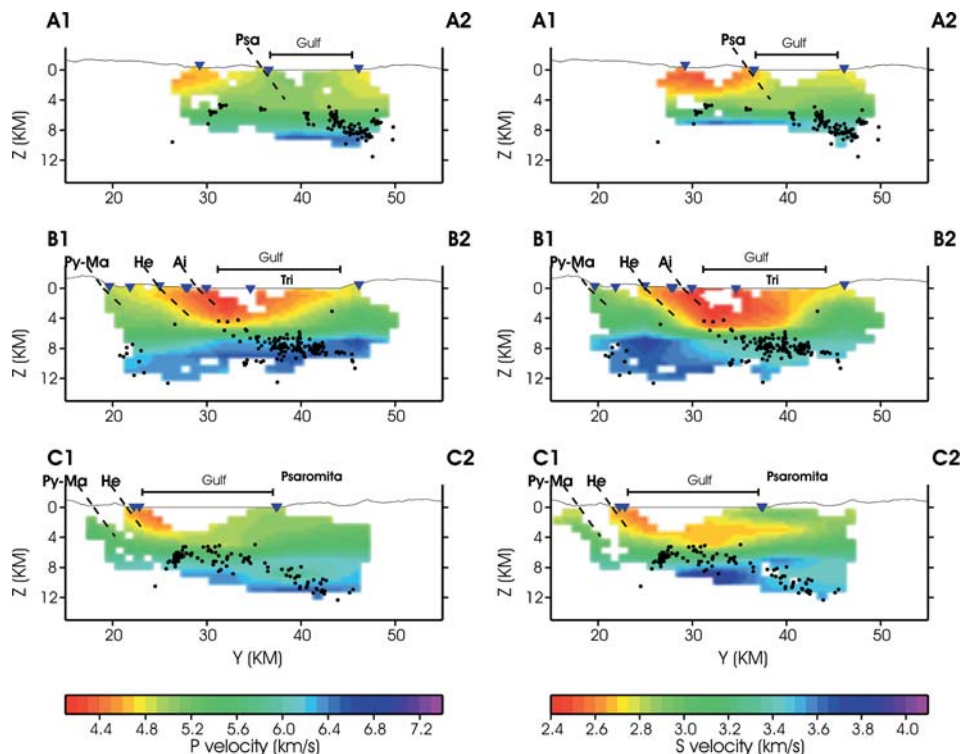


Figure 9

S-N sections of the tomographic results, respectively the P-velocity distribution on the left and the S-velocity model on the right. The location of each S-N section is indicated on Figure 8. Major normal faults are displayed on the pictures. We used the same mask as for the map views.

the same strike when the depth increases. The S-N sections also suggest that events trend along a low-angle dipping surface. This trend is clearly highlighted by projecting earthquakes on a vertical plane orthogonal to the  $120^\circ$  NW-SE direction given by the map view. Figure 11 points out that the microseismicity is aligned along a well-defined  $20^\circ$  north-dipping plane. It is a major result because previous studies did not precisely image this low-angle structure in three dimensions. Contrary to 1991, the seismic activity during the 2002 experiment was very quiet, allowing us to monitor the background microseismicity of the area. Finally, the C1-C2 section (Fig. 9) reveals that the microseismicity is localized in the low  $V_p$  and  $V_s$  anomalies observed at 8–12 km depth beneath the Psaromita area. Spike tests indicate that these anomalies do not correspond to an artefact. The position is well resolved but the amplitude can be underestimated.

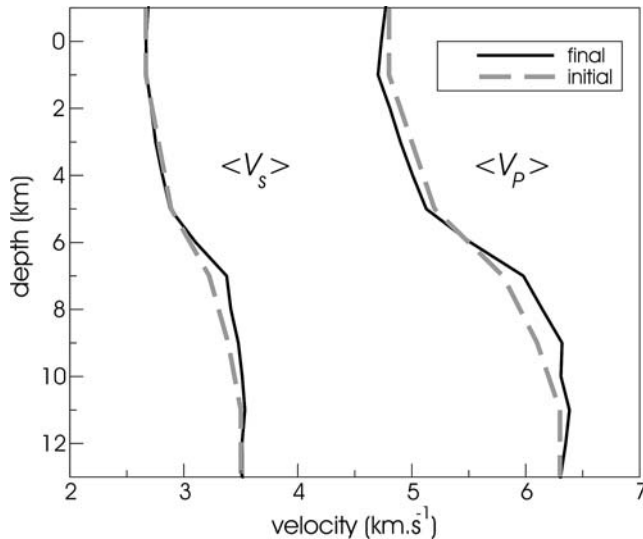


Figure 10

Mean velocity profiles,  $V_s$  on the left and for  $V_p$  on the right, estimated for both the initial model and the tomographic results, taking into account the mask of uncovered areas shown on Figure 8.

### 5.3 Three-dimensional Deduced $V_p.V_s$ and $V_p/V_s$ Models

Images of  $V_p.V_s$  and  $V_p/V_s$  parameters have been deduced from the tomographic models  $V_p$  and  $V_s$ . As previously done by LATORRE *et al.* (2004b), we have checked that these parameters are also at the minimum rms misfit by performing an independent inversion using  $V_p/V_s$  and  $V_p.V_s$  as original parameters. Results are presented on the three S-N sections shown in Figure 12. These two new models bring qualitative information about the distribution of rock properties at depth. For a given lithology, these two parameters are sensitive to porosity and fluid saturation (SANDERS *et al.*, 1995; LEES and WU, 2000; LATORRE *et al.*, 2004b; VANORIO *et al.*, 2005). In particular, low  $V_p.V_s$  values may be related to a high fractured zone whereas high  $V_p/V_s$  values can be explained by fluid saturation. Taking into account the intense seismicity and a possible role of fluids suggested by some authors (RIETBROCK *et al.*, 1996; BERNARD *et al.*, 1997; LATORRE *et al.*, 2004b), these two parameters might provide new constraints for the geodynamic interpretation in the Corinth region.

$V_p.V_s$  images emphasize the two-layer vertical structure with a high  $V_p.V_s$  gradient lying at 5–7 km depth, increasing from  $\sim 15$  ( $\text{km.s}^{-1}$ )<sup>2</sup> to  $\sim 19$  ( $\text{km.s}^{-1}$ )<sup>2</sup>. The shallower part is characterized by a low  $V_p.V_s$  anomaly ( $\sim 11$  ( $\text{km.s}^{-1}$ )<sup>2</sup>) probably related to the structure of the graben. Strong lateral variations of  $V_p.V_s$  are observed in the deeper part. In particular, the S-N sections point out a low  $V_p.V_s$  anomalous zone located northward between 8 km and 12 km depth. This anomaly is clearly

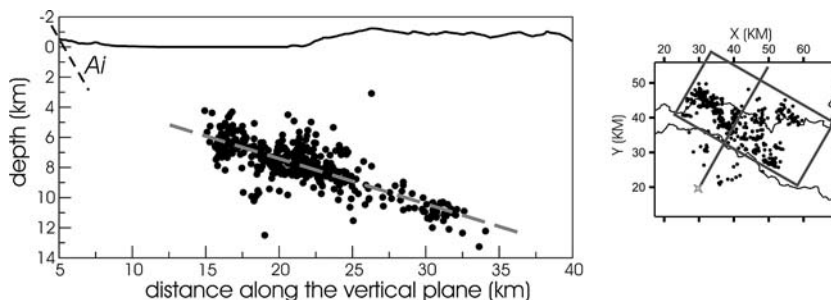


Figure 11

Projection of events located in a given area along a vertical plane orthogonal to the N-120° E orientation of the half-graben. The dashed grey line shows the result of a linear regression. The orientation of the vertical plane and the given area is indicated on the right on a map view. We chose this grey box in order to remove events located beneath the Peloponnesus, which are probably not related to the rifting process. The cross represents the origin of the distance computed along the vertical plane.

observed beneath the Psaromita area (Fig. 12, section C1-C2), where the microseismicity is concentrated in the low anomalous area. The  $V_p/V_s$  pictures show a high anomaly beneath the northern edge of the Gulf at 8–12 km depth (Fig. 12, sections A1–12 and B1–B2), while another positive anomaly is observed at 3–4 km depth (Fig. 9, section C1–C2). We note that events are localized inside the high  $V_p/V_s$  and low  $V_p/V_s$  zone at around 8–12 km depth.

## 6. Discussion and Conclusion

The 2002 data set has provided 3-D and high-resolved images of the mid-crust for the Aigion area. The tomographic models point out a two-layer vertical structure of the mid-crust, existing at a regional scale. The presence of this structure is emphasized by a high velocity gradient lying at 5–7 km depth. These results are in agreement with previous tomographic images obtained from the 1991 data set (LATORRE *et al.*, 2004b). As proposed by LATORRE *et al.* (2004b), this abrupt transition may describe a lithological contact between two different tectonic units of the Hellenic orogenic belt: the Gavrovo-Tripolitza carbonate unit in the upper part and the Phyllite series in the deeper part. By following this interpretation, our tomographic models show that the Gavrovo-Tripolitza nappes may extend down to 5–7 km depth, in accordance with the thickness estimation of the upper series (AUBOUIN *et al.*, 1962). Taking into account the structural position of the Phyllite series beneath the Gavrovo-Tripolitza unit in the Hellenides nappes system (e.g., JACOBSHAGEN *et al.*, 1978) and its presence in a tectonic window, south of the studied area (XYPOLIAS and KOUKOUVELAS, 2001), many authors assume the presence of the Phyllite unit beneath the Gulf of Corinth (PHAM *et al.*, 2000; LATORRE *et al.*, 2004b). In the deeper part of the tomographic models, velocity values are consistent with

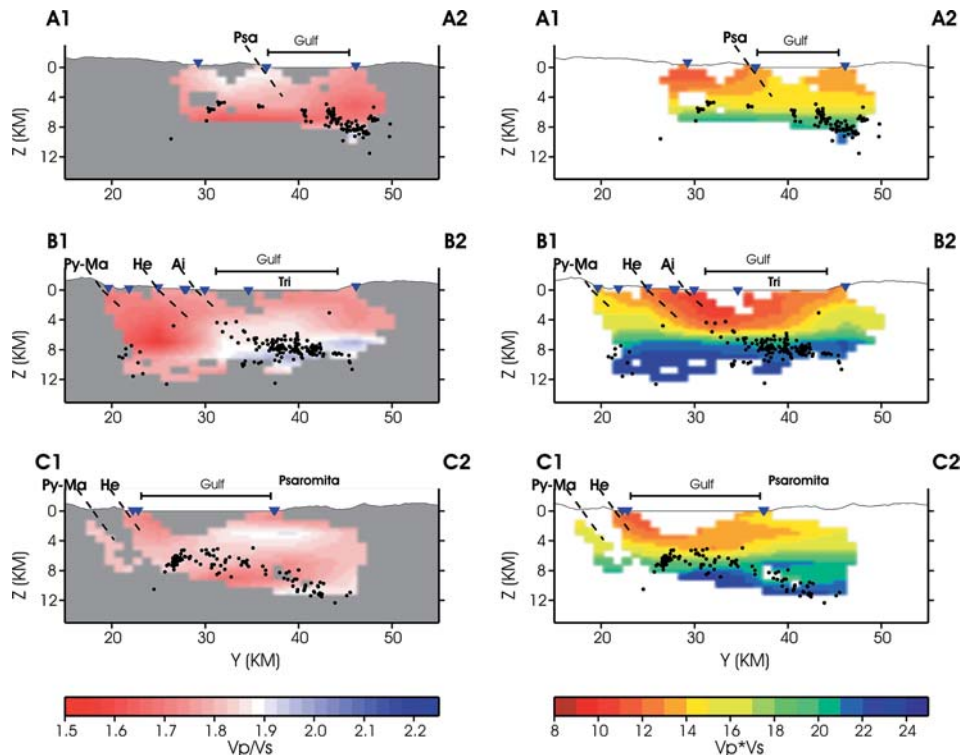


Figure 12

S-N sections of the deduced parameters  $V_p/V_s$  ratio (left) and  $V_p.V_s$  (right). See Figure 8 for location of the three sections. As in previous figures, main faults are indicated by dashed lines, stations are represented by blue triangles and events by dark dots.

velocity estimations of Phyllite rocks obtained from seismic refraction experiments and core measurements (CHRISTENSEN and MOONEY, 1995; CHRISTENSEN, 1996). This supports the assumption of the presence of the Phyllite unit at depth greater than 7 km.

In the shallow crust, the velocity distribution seems to be controlled by the still active extension regime. The low velocity anomaly located beneath the Gulf is found parallel to the graben structure. On the southern side, the low-velocity zone is spatially correlated with the major faults, in particular the Heliki fault. Because this result is consistent with the 1991 tomographic images (LATORRE *et al.*, 2004b), we can consider this low-velocity anomaly as a well-constrained structure. The trend, the position and the velocity values ( $V_p$ ,  $V_s$  and  $V_s.V_s$ ) of this anomaly might be explained both by the presence of thick synrift deposits and the existence of highly fractured carbonates in the first 3 km. This assumption is supported by geological observations (DOUSOS and POULIMENOS, 1992; FLOTTÉ and SOREL, 2001), reflection

seismic images (SACHPAZI *et al.*, 2003) and magneto-telluric modelling (PHAM *et al.*, 2000). Moreover, the 2002 tomographic results presented in this paper clearly confirm the lack of microseismicity in the shallower part, in accordance with long-term seismological observations (LYON-CAEN *et al.*, 2004). This is probably due to a low level of stress in this layer, except near major faults.

The background microseismicity marks a WNW-ESE surface dipping 20°N and lying at 5–13 km depth beneath the Gulf. The event distribution moves from the S-W to the N-E along this surface when the depth increases. Low-dip angle ( $\leq 20^\circ$ ) normal structures with a W-E strike were already observed by previous seismological studies (RIGO *et al.*, 1996; RIETBROCK *et al.*, 1996), but no SW-NE-trending distribution was detected. Differences in direction and in dip can be related to differences in the data set and in the velocity models. In order to determine the events location, these authors used a 1-D-velocity model (RIGO *et al.*, 1996), which does not take into account the lateral variations of the medium. On the contrary, the high quality of the 2002 data set and the 3-D tomography provide a well-constrained image of the low-angle structure, which might be interpreted as a low-angle detachment zone. The extension of the shallower anomaly down to 4–5 km depth is the sole information suggesting that the outcropped faults, here the Heliki fault, are connected with this seismogenic zone (RIGO *et al.*, 1996).

The identified low-angle dipping structure is parallel to the graben axis, indicating a contribution in the deformation of the Gulf region. This result would favor a geodynamic interpretation with two major tectonic phases (TIBERI *et al.*, 2000, 2001): 1) The Miocene extension involving crustal thinning and 2) a reactivation of the rift 1 Ma ago, in a more westward direction. The observed WNW-ESE low-dip surface is in good agreement with this scenario, which postulates that a low-angle detachment could accommodate the offset between the maximum crustal thinning and the graben structure in the western part of the Gulf. Moreover, the SW-NE distribution of the events along the low-dip surface might be related to the westward propagation of the rift.

The tomographic images also point out that the event distribution is consistent with the position of the low P- and S-velocity anomalies observed in the deeper layer (Fig. 9, section C1-C2). This indicates that the low-angle structure does not match the transition zone between the shallower and the deeper layer (HATZFELD *et al.*, 2000; LATORRE *et al.*, 2004b), but crosses this discontinuity. The low-velocity anomalies coupled with a decrease of the  $V_p/V_s$  parameter, may be associated with the presence of a highly fractured zone at 8–12 km depth. The presence of a highly fractured zone can support the assumption of a circulation of deep fluids. This could explain the high  $V_p/V_s$  anomalies observed in the deeper layer on the tomographic images. Fluids may play an important role in the mechanism of the rupture because they may reduce the friction coefficient, allowing seismic slip along the low-angle detachment. This cause has been previously advocated by RIETBROCK

*et al.* (1996) to explain the existence of the low-angle normal fault zone beneath the Gulf of Corinth.

Our results provide new insights on the geodynamic framework of this region. The 3-D velocity models will be used to locate events recorded by the permanent network CRLnet (LYON-CAEN *et al.*, 2004) in order to obtain a precise description of the active structures between Aigion and Trizonia Island. The next step will be a 4-D time-lapse imaging of the area. Deploying the same geometrical network of sensors will help us to design differential tomography if natural sources are found in proximity between these two experiments. Our tomographic models could then be used as the reference frame and one may hope to point out possible time-variations of specific parameters as was done for reservoir engineering. Consequently, comparative studies may bring further key elements for geodynamic modelling.

### *Acknowledgements*

We are grateful to two anonymous reviewers for their critical reviews, which have improved the original manuscript. This work was performed through funding of the European 3F-Corinth Project (ENK6-CT-2000-00056), the French GDR Corinth and the Egide Projects. Partial support has been provided by the CNRS with a post-doctoral fellowship.

### REFERENCES

- AKI, K. and LEE, W. (1976), *Determination of three-dimensional velocity anomalies under a seismic array using first P-arrival times from local earthquakes*, *J. Geophys. Res.* *81*, 4381–4399.
- ARMIJO, R., MEYER, B., KING, G., RIGO, A., and PAPANASTASSIOU, D. (1996), *Quaternary evolution of the Corinth Rift and its implication for the late Cenozoic evolution of the Aegean*, *Geophys. J. Int.* *126*, 11–53.
- AUBOUIN, J., BRUNN, J., CELET, P., DERCOURT, J., GODFRIAUX, I., and MERCIER, J. (1962), *Esquisse de la géologie de la Grèce*, *Mém. Hors Sér. Soc. Géol. France* *2*, 583–610.
- AVALLONE, A., BRIOLE, P., AGATZA-BALODIMIOU, A., BILLIRIS, H., CHARADE, O., MITSAKAKI, C., NERCESSIAN, A., PAPAZISSI, K., PARADISSIS, D., and VEIS, G. (2004), *Analysis of eleven years of deformation measured by GPS in the Corinth Rift laboratory area*, *C. R. Geoscience* *336*, 301–311.
- BENZ, H.M., CHOUET, S.A., DAWSON, P.B., LAHR, J.C., PAGE, R.A., and HOLE, J.A. (1996), *Three-dimensional P- and S-wave velocity structure of Redoubt Volcano, Alaska*, *J. Geophys. Res.* *101*, 8111–8128.
- BERNARD, P., BRIOLE, P., MEYER, B., LYON-CAEN, H., GOMEZ, J.-M., TIBERI, C., BERGE, C., CATTIN, R., HATZFELD, D., LACHET, C., LEBRUN, B., DESCHAMPS, A., COURBOULEX, F., LARROQUE, C., RIGO, A., MASSONET, D., PAPADIMITRIOU, P., KASSARAS, J., DIAGOURTAS, D., MAKROPOULOS, K., VEIS, G., PAPAZISI, E., MITSAKAKI, C., KARAKOSTAS, V., PAPADIMITRIOU, E., PAPANASTASSIOU, D., CHOULIARAS, M., and STAVRAKAKIS, G. (1997), *A low angle normal fault earthquake: the Ms = 6.2, June, 1995 Aigion earthquake (Greece): Evidence for a low-angle normal faulting in the Corinth Rift*, *J. Seismol.* *1*, 131–150.
- BEN-ZION, Y. and MALIN, P. (1991), *San Andreas fault zone head waves near Parkfield, California*, *Science* *251*, 1592–1594.
- BRIOLE, P., RIGO, A., LYON-CAEN, H., RUEGG, J.-C., PAPAZISSI, K., MISTAKAKI, C., BALODIMIOU, A., VEIS, G., HATZFELD, D., and DESCHAMPS, A. (2000), *Active deformation of the Gulf of Korinthos, Greece: Results from repeated GPS surveys between 1990 and 1995*, *J. Geophys. Res.* *105*, 25605–25625.

- CHRISTENSEN, N. and MOONEY, W.D. (1995), *Seismic velocity structure and composition of the continental crust: A global view*, J. Geophys. Res. 100, 9761–9788.
- CHRISTENSEN, N. (1996), *Poisson's ratio and crustal seismology*, J. Geophys. Res. 101, 3139–3156.
- CLARK, P.J., DAVIES, R.R., ENGLAND, P.C., PARSONS, B.E., BILLIRIS, H., PARADISSIS, D., VEIS, G., DENYS, P.H., CROSS, P.A., ASHKENAZI, V., and BINGLEY, R. (1997), *Geodetic estimate of seismic hazard in the Gulf of Corinthos*, Geophys. Lett. 24, 1303–1306.
- DORNSIEPEN, U.F., MANUTSOGLU, E., and MERTMANN, D. (2001), *Permian-Triassic paleogeography of the external Hellenides*, Paleogeog. Paleoclimat. Paleoecol. 172, 327–338.
- DOUSOS, T., KONTOPOULOS, N., and POULIMENOS, G. (1988), *The Corinth-Patras rift as the initial stage of the continental fragmentation behind an active island arc (Greece)*, Basin Research 1, 177–190.
- DOUSOS, T. and POULIMENOS, G. (1992), *Geometry and kinematics of active faults and their seismotectonic significance in the western Corinth-Patras rift (Greece)*, J. Struct. Geol. 14, 689–699.
- FLOTTÉ, N. and SOREL, D. (2001), *Structural cross sections through the Corinth-Patras detachment fault-system in Northern Peloponnesus (Aegean Arc, Greece)*, Bull. Geol. Soc. Greece XXXIV, 235–241.
- HATZFELD, D., KARAKOSTAS, V., ZIAZIA, M., KASSARAS, I., PAPADIMITRIOU, E., MAKROPOULOS, K., VOULGARIS, N., and PAPAIOANNOU, C. (2000), *Microseismicity and faulting geometry in the Gulf of Corinth (Greece)*, Geophys. J. Int. 141, 438–456.
- JACOBSSHAGEN, V., DURR, V., KOCKEL, F., KOPP, K.O., KOWALCZYK, G., BERCKHEMER, H., and BUTTNER, D. (1978), *Structure and geodynamic evolution of the Aegean Region*. In *Alpes Apennines Hellenides* (eds. Closs H., Roeder D., Schmidt K.) (Schweiz-Verlag, 1978) pp. 537–564.
- JOLIVET, L., BRUN, J.P., GAUTIER, P., LALLEMEANT, S., and PATRIAT, M. (1994), *3D-kinematics extension in the Aegean region from the early Miocene to the present, insight from the ductile crust*, Bul. Soc. Geol. France 165, 195–209.
- JOLIVET, L. (2001), *A comparison of geodetic and finite strain pattern in the Aegean, geodynamic implications*, Earth Planet Sci. Lett. 187, 95–104.
- KISSLING, E., ELLSWORTH, W.L., EBERHART-PHILLIPS, D., and KRADOLFER, U. (1994), *Initial reference models in local earthquake tomography*, J. Geophys. Res. 99, 19635–19646.
- LATORRE, D., VIRIEUX, J., MONFRET, T., and LYON-CAEN, H. (2004a), *Converted seismic wave investigation in the Gulf of Corinth from local earthquakes*, C.R Geosciences 336, 259–267.
- LATORRE, D., VIRIEUX, J., MONFRET, T., MONTEILLER, V., VANORIO, T., GOT, J.-L., and LYON-CAEN, H. (2004b), *A new seismic tomography of Aigion area Gulf of Corinth, Greece from a 1991 data set*, Geophys. J. Int. 159, 1013–1031.
- LEE, J.M. and WU, H. (2000), *Poisson's ratio and porosity at Coso geothermal area, California*, J. Volcanol. Geotherm. Res. 95, 157–173.
- LE MEUR, H., VIRIEUX, J., and PODVIN, P. (1997), *Seismic tomography of the Gulf of Corinth: A comparison of methods*, Ann. Geophys. XL, 1–25.
- LE PICHON, X. and ANGELIER, J. (1979), *The Hellenic arc and trench system: A key to the neotectonic evolution of the eastern Mediterranean area*, Tectonophysics 60, 1–42.
- LE PICHON, X., CHAMOT-ROOKE, N., LALLEMANT, S. (1995), *Geodetic determination of the kinematics of central Greece with respect to Europe: Implications for eastern Mediterranean tectonics*, J. Geophys. Res. 100, 12675–12690.
- LYON-CAEN, H., PAPADIMITRIOU, P., DESCHAMPS, A., BERNARD, P., MAKROPOULOS, K., PACCHIANI, F., and PATAU, G. (2004), *First results of the CRLN seismic array in the western Corinth rift: Evidence for old fault reactivation*, C. R. Geoscience 336, 343–351.
- MCCCLUSKY, S., BALASSANIAN, S., BARKA, A., DEMIR, C., ERGINTAV, S., GEORGIEV, I., GURKAN, O., HAMBURGER, M., HURST, K., KAHLE, H., KASTENS, K., KEKELIDZE, G., KING, R., KOTZEV, V., LENK, O., MAHMOUD, S., MISHIN, A., NADARIYA, M., OUZOUNIS, A., PARADISSIS, D., PETER, Y., PRILEPIN, M., REILINGER, R., SANLI, I., SEEGER, H., TEALEB, A., TOKSÖZ, M.N., and VEIS, G. (2000), *Global Positioning System constraints on plate kinematics and dynamics in the eastern Mediterranean and Caucasus*, J. Geophys. Res. 105, 5695–5719.
- MONTEILLER, V., GOT, J.L., VIRIEUX, J., and OKUBO, P., *An efficient algorithm for double-difference tomography and location in heterogeneous media, with an application to Kilauea volcano*, J. Geophys. Res., in press.
- MOSEGAARD, K. and TARANTOLA, A. (1995), *Monte Carlo sampling of solutions to inverse problems*, J. Geophys. Res. 100, 12431–12447.

- PAIGE, C.C. and SAUNDERS, M.A. (1982), *LSQR: An algorithm for sparse linear equations and sparse least squares*, ACM Trans. Math. Software 8, 43–71.
- PHAM, V.N., BERNARD, P., BOYER, D., CHOULIARAS, G., MOUEL, J.L.L., and STAVRAKAKIS, G.N. (2000), *Electrical conductivity and crustal structure beneath the Central Hellenides around the Gulf of Corinth (Greece) and their relationship with the seismotectonics*, Geophys. J. Int. 142, 948–969.
- PODVIN, P. and LECOMTE, I. (1991), *Finite difference computation of travel-time in very contrasted velocity model: A massively parallel approach and its associated tools*, Geophys. J. Int. 105, 271–284.
- RIETBROCK, A., TIBERI, C., SCHERBAUM, F., and LYON-CAEN, H. (1996), *Seismic slip on a low angle normal fault in the Gulf of Corinth: Evidence from high-resolution cluster analysis of microearthquakes*, Geophys. Res. Lett. 23, 1817–1820.
- RIGO, A., LYON-CAEN, H., ARMIJO, R., DESCHAMPS, A., HATZFELD, D., MAKROPOULOS, K., PAPADIMITRIOU, P., and KASSARAS, I. (1996), *A microseismic study in the western part of the Gulf of Corinth (Greece): Implications for large-scale normal faulting mechanisms*, Geophys. J. Int. 126, 663–688.
- SACHPAZI, M., CLÉMENT, C., LAIGLE, M., HIRN, A., and ROUSSOS, N. (2003), *Rift structure, evolution, and earthquakes in the Gulf of Corinth, from reflection seismic images*, Earth Planet. Sci. Lett. 216, 243–257.
- SANDERS, C.O., PONKO, S.C., NIXON, L.D., and SCHATZ, E.A. (1995), *Seismological evidence for magmatic and hydrothermal structure in Long Valley caldera from local earthquake attenuation and velocity tomography*, J. Geophys. Res. 100, 8311–8326.
- SOREL, D. (2000), *A Pliocene and still-active detachment fault and the origin of the Corinth-Patras rift, Greece*, Geology 28, 83–86.
- SPAKMAN, W. and NOLET, G., *Imaging algorithms, accuracy and resolution*, In *Mathematical Geophysics* (ed. Vlaar N.) (D. Reidel Publ. Co., Dordrecht 1988) pp. 155–187.
- SPENCER, C.P. and GUBBINS, D. (1980), *Travel-time inversion for simultaneous earthquake location and velocity structure determination in laterally varying media*, Geophys. J. R. Astron. Soc. 63, 95–116.
- TIBERI, C., LYON-CAEN, H., HATZFELD, D., ACHAUER, U., KARGIANNI, E., KIRATZI, A., LOUVARI, E., PANAGIOTOPOULOS, D., KASSARAS, I., KAVIRIS, G., MAKROPOULOS, K., and PAPADIMITRIOU, P. (2000), *Crustal and upper mantle structure beneath the Corinth rift (Greece) from a teleseismic tomography study*, J. Geophys. Res. 105, 28159–28171.
- TIBERI, C., DIAMENT, M., LYON-CAEN, H., and KING, T. (2001), *Moho topography beneath the Corinth rift area (Greece) from inversion of gravity data*, Geophys. J. Int. 145, 797–808.
- THURBER, C.H. (1992), *Hypocenter-velocity structure coupling in local earthquake tomography*, Phys. Earth Planet Inter. 75, 55–62.
- VANORIO, T., VIRIEUX, J., CAPUANO, P., and RUSSO, G. (2005), *Three-dimensional seismic tomography from P-wave and S-wave microearthquake travel times and rock physics characterization of the Campi Flegrei Caldera*, J. Geophys. Res. 110, B03201, 10.1029/2004JB003102.
- XYPOLIAS, P. and KOUKOUVELAS, I. (2001), *Kinematics vorticity and strain rate patterns associated with ductile extrusion in the Chelmos Shear Zone (External Hellenides, Greece)*, Tectonophysics 338, 59–77.

(Received April 4, 2005; accepted September 23, 2005)

Published Online First: February 8, 2006



To access this journal online:

<http://www.birkhauser.ch>

---